"Calibration of Monte Carlo Charge Transport Simulation Parameters"

CONTRACT: HQ0006-06-C-7519

Final Report – May/2007
Douglas Yoder, PI

Introduction and Motivation

As a consequence of favorable macroscopic material properties such as thermal conductivity, piezoelectricity, breakdown field, and electron mobility, wurtzite III-nitride materials are currently being pursued for a plethora of diverse applications, including RF power amplification[1,2], power switching[3], surface acoustic wave chemical and biological sensors[4], solar-blind photodetectors[5], as well as lasers and light emitting diodes in the green to deep UV range[6,7]. Although the performance of many of these devices has been superlative, the wurtzite III-nitrides are a relatively new material system, and our knowledge of some of their more fundamental material properties is still incomplete at best. Additionally, issues associated with material quality such as dislocations, point defects, clustering, etc., may influence device operation. These considerations naturally limit the precision of our understanding of device operation, and pose a significantly greater challenge to the simulation of III-nitride devices than would be the case for any of the more mature material systems.

In this study, static I/V characteristics of the present 0.25 μm short-gate AlGaN/GaN HFET technology are analyzed, and used to refine our understanding of microscopic material parameters required as input for fall band Monte Carlo device simulation. The Monte Carlo technique is a stochastic method for the exact solution of the semi-classical Boltzmann Transport Equation (BTE). The trajectories of a representative sample of electrons in a given HFET are tracked through a multi-dimensional phase space[8], under the influence of inhomogeneous built-in and applied fields, as well as elastic and inelastic scattering mechanisms. Electronic dispersion is calculated using the non-local empirical pseudopotential technique[9]. Both local and non-local atomic pseudopotentials are optimized such that calculated optical transition energies and effective masses conform to known values. The result for GaN is shown in Figure 1.

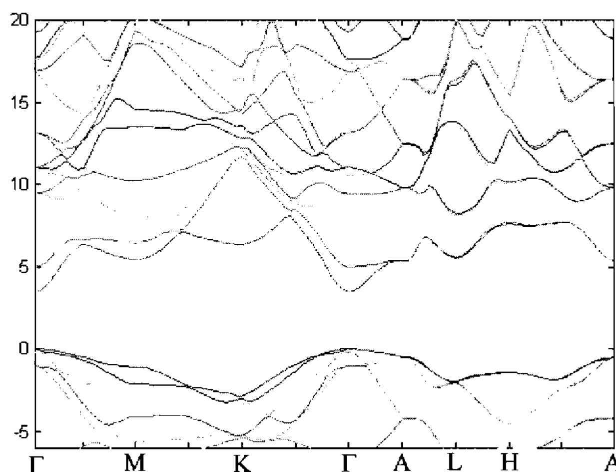

Figure 1: Electronic dispersion of wurtzite GaN. Vertical axis: electron energy (eV). Horizontal axis: crystal momentum.

Description of Scattering Mechanisms

Scattering mechanisms considered in our simulations include the anisotropic polar optic interaction, the deformation potential interaction, piezoelectric scattering, charged impurity scattering, and dislocation scattering:

Polar Optic Interaction:

The Froehlich interaction Hamiltonian for wurtzite crystals assumes a particularly anisotropic form, compared to the more familiar expressions for zincblende materials. Second quantizing the phonon field, we write:

$$\hat{\mathrm{H}} = \sum_{\vec{q}} \left(\frac{4\pi e^2 \hbar}{2q^2 \Omega \omega_{\vec{q}}} \right)^{0.5} \frac{\left(b_{\vec{q}} + b^{*}_{-\vec{q}}\right) e^{i(\vec{q}\cdot\vec{r} - \omega_{\vec{q}} t)} (\omega_{\perp T}^2 - \omega_{\vec{q}}^2)(\omega_{zT}^2 - \omega_{\vec{q}}^2)}{\left(q_\perp^2 \omega_{\perp T}^2 (\omega_{zT}^2 - \omega_{\vec{q}}^2)(\varepsilon_\perp^0 - \varepsilon_\perp^\infty) + q_z^2 \omega_{zT}^2 (\omega_{\perp T}^2 - \omega_{\vec{q}}^2)(\varepsilon_\perp^0 - \varepsilon_\perp^\infty)\right)^{0.5}},$$

where $\vec{q}$ indicates the phonon wave vector, the symbol ω represents phonon angular frequency, and the subscripts "z" and "$\perp$" refer to the directions parallel and perpendicular to the crystal's c-axis, respectively. As is the case in zincblende crystals, a strong polar-optic interaction exists between electrons and LO-polarized phonons in wurtzite materials. Because the wurtzite lattice lacks inversion symmetry, a polar-optic interaction is also possible with TO_2 phonons. In practice, however, this latter interaction is of negligible magnitude compared to the former, and is neglected in the present work. The differential polar-optic scattering rate due to LO phonons follows from first order perturbation theory, and takes the following form:

$$S(\vec{k},\vec{k}') = \frac{2\pi}{\hbar} \left(\frac{4\pi e^2 \hbar}{2q^2 \Omega \omega_{\vec{q}}} \right) \left[\frac{q_\perp^2}{\frac{\varepsilon_\perp^0 - \varepsilon_\perp^\infty}{\varepsilon_\perp^0 \varepsilon_\perp^\infty} q^2 \omega_{\perp L}^2} + \frac{q_z^2}{\frac{\varepsilon_z^0 - \varepsilon_z^\infty}{\varepsilon_z^0 \varepsilon_z^\infty} q^2 \omega_{zL}^2} \right]^{-1} \left(N_{\vec{q}} + \frac{1}{2} \pm \frac{1}{2} \right) I(\vec{k},\vec{k}') \delta\left(E_{n'}(\vec{k}') - E_n(\vec{k}) \pm \hbar\omega_{\vec{q}} \right)$$

where the function I(k,k') denotes the square of the usual overlap integral. In the present work, we have adopted the approximate expression $\omega_{LO}^2 = \omega_{zL}^2 \cos^2\theta + \omega_{\perp L}^2 \sin^2\theta$ to describe the anisotropy of the LO mode phonon, in which the symbol θ represents the angle of the phonon wave vector with respect to the c-axis. In our Monte Carlo implementation, final states for scattered electrons are selected according to the exact anisotropic transition probabilities, and are consistent with the full pseudopotential band structure. In the interest of efficient simulation, however, we detect for scattering events themselves with an energy-dependent total polar-optic scattering rate, where the above equation is integrated not just over final states, but also over all initial states on each iso-energy surface.

Piezoelectric Interaction:

Polarization of the crystal lattice also arises due to the strain field of acoustic phonons. In the case of the wurtzite lattice, both the LA and TA_2 modes may exchange energy and momentum

with electrons, though the influence of the (in-plane) acoustic mode is usually larger. In terms of phonon polarization $\vec{\eta}$ and wave vector $\vec{q}$, the intravalley transition rates may be written as:

$$S(\vec{k},\vec{k}')=\frac{2\pi}{\hbar}\left(\frac{\hbar}{2\rho\Omega\omega_{\vec{q}}}\right)\frac{(\vec{\eta}_{\perp}\cdot\vec{q}_{\perp})q_z(\bar{e}_{15}+\bar{e}_{31})+\eta_z(q_{\perp}^2\bar{e}_{15}+q_z^2\bar{e}_{33})}{q^2}\left(N_{\vec{q}}+\frac{1}{2}\pm\frac{1}{2}\right)I(\vec{k},\vec{k}')\delta\left(E_{n'}(\vec{k}')-E_n(\vec{k})\pm\hbar\omega_{\vec{q}}\right)$$

where the symbol ρ indicates the crystal mass density, and the normalized piezoelectric coefficients are defined as $\bar{e}_{15}=ee_{15}/\varepsilon_{\perp}^0$, $\bar{e}_{33}=ee_{33}/\varepsilon_z^0$, *and* $\bar{e}_{31}=ee_{31}/\varepsilon_z^0$.

Deformation Potential Interaction:

All lattice vibrations represent a spatiotemporal deformation of the crystal lattice (whether or not they generate a macroscopic polarization field), perturbing the local atomic potentials. Such perturbations in the crystal potential tend to be of relatively short range, and may scatter charge carriers through a deformation potential interaction, as originally proposed by Bardeen. In contrast to piezoelectric and polar-optic scattering, the deformation potential interaction can lead to quite large inter-valley and inter-band transition rates. For a given phonon polarization $\vec{\eta}$, the differential transition rate due to the deformation potential interaction may be written as

$$S(n\vec{k},n'\vec{k}')=\frac{2\pi}{\hbar}\left(\frac{\hbar}{2\rho\Omega\omega_{\vec{\eta},\vec{q}}}\right)\left|D_{\vec{\eta}}(n\vec{k},n'\vec{k}')\right|^2\left(N_{\vec{q}}+\frac{1}{2}\pm\frac{1}{2}\right)\delta\left(E_{n'}(\vec{k}')-E_n(\vec{k})\pm\hbar\omega_{\vec{\eta},\vec{q}}\right),$$

Where $D_{\vec{\eta}}(n\vec{k},n'\vec{k}')$ is the so-called deformation potential. The complexity of the deformation potential $D_{\vec{\eta}}(n\vec{k},n'\vec{k}')$ is tremendous, and impractical to account for exactly in simulations for engineering applications. For this reason, we treat the deformation potential as a piecewise constant function of $(n\vec{k},n'\vec{k}')$, with discontinuities only at boundaries between adjacent valleys and across bands. For this purpose, we partition the Brillouin zone into "regions" associated with the Γ, A, H, L, M, and K valleys. Electron scattering rates are then calculated in a manner consistent with the full pseudopotential band structure, using a table of intravalley, intraband, intervalley and interband deformation potentials, accounting for relevant phonon modes.

Dislocation Scattering:

Growth of GaN and related compound semiconductors on lattice mismatched substrates is well known to introduce extended defects with localized electronic states lying within the band gap. It has been experimentally observed that edge and screw dislocations which reach the top epitaxial layers are predominantly vertical, when the active epitaxial layers are grown on a thick transitional buffer layer. Therefore, although localized states associated with dislocations are often filled during normal device operation[10], their electrostatic influence on mobile charge carriers takes on a simple cylindrically-symmetric form, as previously noticed by several authors[11]. Careful analysis yields the following expression for the differential electron scattering rate

$$S(n\vec{k},n'\vec{k}')=\frac{2\pi}{\hbar}N_{2D}\left(\frac{Q_\ell}{\varepsilon q\left(q+q_{TF}\right)}\right)^2\delta(k_z'-k_z)I(\vec{k},\vec{k}')\delta\left(E_{n'}(\vec{k}')-E_n(\vec{k})\right),$$

where N_{2D} is the two-dimensional density of charged dislocations, Q_ℓ is the linear charge density, and the influence of screening by mobile charge is expressed through q_{TF}, the Thomas-Fermi wave vector.

Ionized Impurity Scattering:

Unintentional doping is an undesired by-product of epitaxial growth. Shallow donor-like impurities in intrinsic material are of greatest consequence, and result in a screened Coulombic scattering perturbing potential when ionized. Because if its significance in all semiconductor materials and device technologies, ionized impurity scattering is arguably the most researched scattering mechanism of all. The differential scattering rate due to ionized impurities may be written in the following form:

$$S(n\vec{k},n'\vec{k}') = \frac{2\pi}{\hbar} N_{3D} \left(\frac{e}{q^2 \varepsilon(q,0)} \right)^2 I(\vec{k},\vec{k}')\delta\left(E_{n'}(\vec{k}') - E_n(\vec{k})\right),$$

Where N_{3D} is the density of ionized impurities, and $\varepsilon(q)$ is the zero-frequency wave vector dependent dielectric constant, which accounts appropriately for the screening of the bare ionic potentials due to free carriers.

Simulation Details

Electronic dispersion is pre-tabulated on a fine grid in the irreducible wedge of the Brillouin zone. This k-space grid contains 16373 uniformly distributed vertices, and electronic dispersion is assumed to vary linearly within tetrahedral volume elements. A fine grid in real space, generated according to the octree algorithm using both rectangular and triangular elements is likewise employed to store electrostatic potential and electric field information. The equations of motion for electrons and holes are then solved analytically within each cell in phase space assuming linear variation of tabulated quantities, as has been described elsewhere[12,13], allowing for an exact solution to the Boltzmann transport equation to the accuracy of the phase-space grid. For purposes of this study, we employ a floating ensemble of approximately 2×10^5 particles, and begin simulation for the bias V_{DS}=0 with initial conditions given by the equilibrium distribution. The equilibrium distribution is established under the assumption of a constant Fermi level throughout the GaN region of the device. Electrostatic Dirichlet boundary conditions are applied in a manner consistent with a Schottky gate contact, and ohmic source and drain contacts.

Internal to the device domain, the displacive ferroelectricity of wurtzite III-nitride material leads to a spontaneous electrical polarization along the crystalline c-axis; the magnitude of this spontaneous polarization is known[14], and we model it with the introduction of fixed surface charge at each material interface. Likewise, the biaxial tensile strain in the AlGaN barrier material introduces a piezoelectric polarization[15] along the c-axis, also modeled by means of fixed surface charge. For purposes of device simulation, both spontaneous and piezoelectric fixed surface charge is incorporated into the 2D Poisson equation as an additional source term on the right hand side at each relevant interface vertex, and solutions are sought according to the box discretization scheme. Subsequent simulations at higher drain-source bias are seeded with initial conditions given by the converged electron distribution from the previous bias point. For

each bias point, particle trajectories are computed beginning at time t=0, and synchronized self-consistently with solutions of the Poisson equation (accounting for internal polarization charges and Dirichlet boundary conditions) on a sub-femtosecond time scale. The motion of charges internal to the device domain induces the flow of current through device contacts, which we calculate rigorously through application of the Ramo-Shockley theorem[16,17]. Throughout the course of each simulation, electron statistics for several common semiclassical observables (e.g. electron density, velocity, average energy, etc.) are collected at each vertex of the real-space grid, and convergent criteria for these estimators determine the length of each simulation.

Results and Discussion:

Deformation potential constants for the electron-phonon interaction have previously been calibrated to reproduce the known bulk velocity-field characteristics in pure GaN for transport in the basal plane. Microscopic scattering parameters specific to Nitronex' submicron gate technology are related to the density of ionized impurities, and the density and occupancy level of dislocations: N_{3D}, N_{2D} and Q_ℓ.

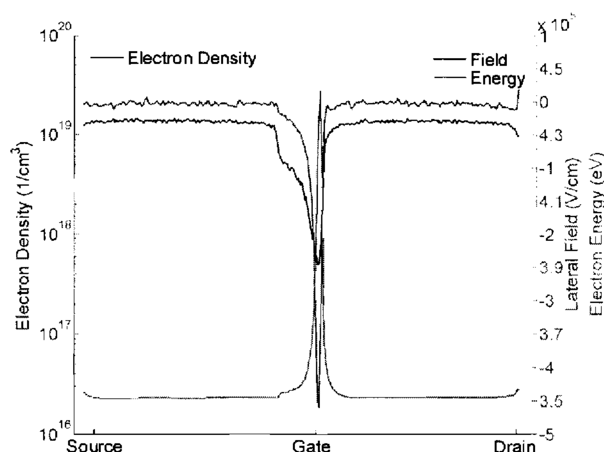

Figure 2: Electron density, average energy, and electric field strength along a longitudinal cut line from source to drain. Vgs=-1V, Vds=3V. The "hot spot" lies just to the right of the peak field strength.

Figure 2 demonstrates the typical spatial variation of electron density, longitudinal electric field, and average electron energy along a one-dimensional path through the channel from source to drain, shown here for the case of a -1V gate bias and 3V drain-source bias. As is common, the peak longitudinal electric field in the channel may be found underneath the gate contact on the drain side. Although the point of largest longitudinal electric field is also the point of lowest electron density in steady-state (as a consequence of current continuity considerations), it is also the point of largest electron velocity and highest average electron energy[18], as the lateral growth in longitudinal field strength accelerates electrons to monotonically increasing energies. For this reason, this point is simultaneously the location of maximum Joule heating, where the rate at which electrons lose energy in the creation of optical phonons is largest. For this reason, this point is often referred to as the "hot spot". The three above mentioned technology-dependent material parameters were adjusted to obtain the best fit to measured D.C. current-voltage relationships at low bias levels. Simulation results are indicated in Figure 3, and were obtained for values of 2×10^{16} cm^{-3} for the unintentional ionized impurity density, 1.5×10^{9} cm^{-2} for the dislocation

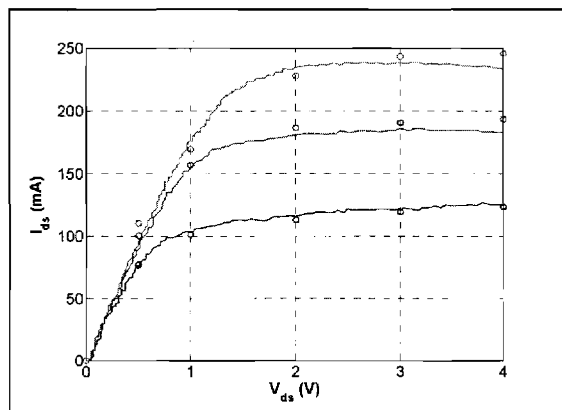

Figure 3: Static current-voltage measurement (solid lines) and Monte Carlo simulation (circles), for VGS = -1, 0 and 1V. Discrepancy at large gate bias is attributable to lattice heating, not considered in the simulations.

density, at an assumed occupancy level of 100%. For a gate bias of -1V, the agreement between measurement and simulation is excellent. At higher channel electron density and high drain-source bias, Joule heating leads to pronounced electrothermal feedback, lowering electron mobility throughout the channel, and ultimately lowering drain current. For the present study, electrothermal feedback has not been considered, and simulation predicts a slightly higher drain current than actually observed in the case of these larger biases.

References

[1] J. W. Johnson, E. L. Piner, A. Vescan, R. Therrien, P. Rajagopal, J. C. Roberts, J. D. Brown, S. Singhal, and K. J. Linthicum, "12W/mm AlGaN HFETs on Silicon Substrates," *IEEE Electron Device Letters*, vol. 25, pp. 459-461, 2004.

[2] T. Palacios, A. Chakraborty, S. Rajan, C. Poblenz, S. Keller, S. P. DenBaars, J. S. Speck, and U. K. Mishra, "High power AlGaN/GaN HEMTs for Ka-band applications," *IEEE Electron Device Letters*, vol. 26, pp. 781-783, 2005.

[3] W. Saito, Y. Takada, M. Kuraguchi, K. Tsuda, I. Omura, T. Ogura, and H. Ohashi, *IEEE Transactions on Electron Devices*, vol. 50, pp. 2528-2531, 2005.

[4] S. J. Pearton, B. S. Kang, S. Kim, F. Ren, B. P. Gila, C. R. Abernathy, J. Lin, and S. N. G. Chu, "GaN-based diodes and transistors for chemical, gas biological and pressure sensing," *Journal of Physics: Condensed Matter*, vol. 16, pp. R961-R994, 2004.

[5] T. Li, D. J. H. Lambert, M. M. Wong, C. J. Collins, B. Yang, A. L. Beck, U. Chowdhury, R. D. Dupuis, and J. C. Campbell, "Low-noise back-illuminated Al_xGa_1_-_xN-based p-i-n solar-blind ultraviolet photodetectors," *IEEE Journal of Quantum Electronics*, vol. 37, pp. 538-545, 2001.

[6] S. Nakamura and G. Farol, *The Blue Laser Diode*. Berlin, Germany: Springer Verlag, 1998.

[7] I. Akasaki and H. Amano, "Breakthroughs in Improving Crystal Quality of GaN and Invention of the p-n Junction Blue-Light-Emitting Diode," *Japanese Journal of Applied Physics*, vol. 45, pp. 9001-9012, 2006.

[8] In the present work, trajectories are computed in two real-space dimensions, three momentum-space dimensions, and time.

[9] J. R. Chelikowsky and M. L. Cohen, *Physical Review B*, vol. 13, pp. 556-582, 1976.

[10] D. C. Look and J. R. Sizelove, *Physical Review Letters*, Vol. 82, pf. 1237, 1999.

[11] N. G. Weimann, L. F. Eastman, D. Doppalapudi, H. M. Ng and J. Moustakis, *Journal of Applied Physics*, Vol 83, pf. 3656, 1998.

[12] J.D. Bude, M.R.Pinto and R.K.Smith, *Semiconductor Science and Technology*, Vol. 9, pp. 840-843, 1994.

[13] F.M. Bufler, P.D. Yoder and W. Fichtner, Proceedings of the 7th Annual Workshop on Computational Electronics, pp. 64-65, 1999.

[14] F. Bernardini and V. Fiorentini, *Physical Review B*, vol. 56, pp. 24-27, 1997.

[15] O. Ombacher, M. Eickhoff, a. Link, M. Hermann, M. Stutzmann, F. Bernardini, V. Fiorentini, Y. Smorchkova, J. Speck, U. Mishra, W. Schaff, V. Tilak and L. F. Eastman, *Physica Status Solidi*, vol. 6, pp. 1878-1907, 2003.

[16] W. Shockley, *Journal of Applied Physics* 9, pp. 635-636, 1938.

[17] P. D. Yoder, K. Gärtner and W. Fichtner, *Journal of Applied Physics*, Vol. 79, pf. 1951, 1996.

[18] In reality, the location of peak longitudinal field, minimum electron density, maximum electron velocity and maximum average electron energy do not occur at exactly the same point along the channel. Their separation is typically on the order of a few nm, which is small compared to the source-drain spacing.

Research Report Approval Sheet

Doc ID: 104148 PS Project #: 2726669 PS Fund #: R7621 Old Project #:

Project Title: CALIBRATION OF MONTE CARLO CHARGE TRANSPORT SIMULATION PARAMETERS

PD/PI(s): YODER, PAUL DOUGLAS (PDPI)/

Sponsor: NITRONEX CORPORATION/RALEIGH, NC **Unit/Lab: GT SAVANNAH**

Deliv ID: 1 Due Date: 31-AUG-2007 **Number of Copies: 1**

Deliverable Title: FINAL REPORT

Period Covered: 28-AUG-2006 through 31-AUG-2007

WebWISE Status: Submitted to OSP **WebWise Mailed Date: 10-Sep-2007**

Status Changed By: YODER,PAUL **Status Changed Date: 10-SEP-2007**

Details Sent to OSP/OCA:

Will PD send a paper copy of the deliverable to OSP (no upload): N

Is Deliverable Classified: N

Is Deliverable Restricted: N

Does OSP need to send the deliverable to sponsor: N

Comments to OSP: I delivered the attached final report to Nitronex in May of this year, at their request. Nitronex already has it. If you need to send this to Nitronex again, it might be confusing, so you should attach a note indicating that this is a document which I already sent them, corresponding to Phase I of our SBIR contract. I am currently working on Phase II with Nitronex. Thanks, Doug

Signatures and Approvals:

PD/PI: ____________________ Date:____________

Division Chief or Branch Head: ____________________ Date:____________

Lab/School/Department/Center Head: ____________________ Date:____________

MAPS/RAN: ____________________ Date:____________

Research Security: ____________________ Date:____________